

# Magnetic field tomography, helical magnetic fields and Faraday depolarization

C. Horellou<sup>1\*</sup> and A. Fletcher<sup>2</sup>

<sup>1</sup> *Department of Earth and Space Sciences, Chalmers University of Technology, Onsala Space Observatory, SE-439 92 Onsala, Sweden*

<sup>2</sup> *School of Mathematics and Statistics, Newcastle University, Newcastle-upon-Tyne NE1 7RU, U.K.*

Accepted 2014 April 6. Received 2014 March 24; in original form 2014 January 16

## ABSTRACT

Wide-band radio polarization observations offer the possibility to recover information about the magnetic fields in synchrotron sources, such as details of their three-dimensional configuration, that has previously been inaccessible. The key physical process involved is the Faraday rotation of the polarized emission in the source (and elsewhere along the wave’s propagation path to the observer). In order to proceed, reliable methods are required for inverting the signals observed in wavelength space into useful data in Faraday space, with robust estimates of their uncertainty. In this paper, we examine how variations of the intrinsic angle of polarized emission  $\psi_0$  with the Faraday depth  $\phi$  within a source affect the observable quantities. Using simple models for the Faraday dispersion  $F(\phi)$  and  $\psi_0(\phi)$ , along with the current and planned properties of the main radio interferometers, we demonstrate how degeneracies among the parameters describing the magneto-ionic medium can be minimised by combining observations in different wavebands. We also discuss how depolarization by Faraday dispersion due to a random component of the magnetic field attenuates the variations in the spectral energy distribution of the polarization and shifts its peak towards shorter wavelengths. This additional effect reduces the prospect of recovering the characteristics of the magnetic field helicity in magneto-ionic media dominated by the turbulent component of the magnetic field.

**Key words:** polarization – methods: data analysis – techniques: polarimetric – ISM: magnetic fields – galaxies: magnetic fields – radio continuum: galaxies

## 1 INTRODUCTION

A new generation of radio telescopes will map the polarization of cosmic radio sources over a large range of wavelengths, from a few centimetres to several metres. Since the plane of polarization of a linearly polarized wave is rotated by an amount that depends on the magnetic field and free-electron distributions and the wavelength ( $\lambda$ ), the resulting data will probe both the synchrotron-emitting sources and any intervening magneto-ionic medium in unprecedented detail. A useful way to characterize the intrinsic properties of magneto-ionic media is the Faraday dispersion function<sup>1</sup>,  $F(\phi)$ , which contains information on the transverse orientation of the magnetic field ( $B_\perp$ ) and on the intrinsic polarized emission as a function of Faraday depth,  $\phi$ . The Faraday depth is proportional to the integral along the line of sight

$z$  of the product of the density of thermal electrons,  $n_e$ , and the component of the magnetic field parallel to the line of sight:

$$\phi(z) \propto \int_z^{+\infty} n_e(z') B_\parallel(z') dz', \quad (1)$$

hence, in principle,  $F(\phi)$  can be used to obtain both the perpendicular and the parallel components of the three-dimensional magnetic field. (Our system of coordinates is such that the origin is at the far end of the source and the observer is located at  $+\infty$ . A magnetic field pointing towards the observer yields a positive Faraday depth.)

Reconstruction of  $F(\phi)$  is usually done by taking advantage of the Fourier-transform type relationship between the observed polarized emission and the Faraday dispersion function. The *observed* complex polarization  $P(\lambda^2)$  can be expressed as the integral over all Faraday depths of the *intrinsic* complex polarization  $F(\phi)$  modulated by the Faraday rotation (Burn 1966):

\* E-mail: cathy.horellou@chalmers.se

<sup>1</sup> The term ‘Faraday spectrum’ is sometimes used for the Faraday dispersion function, which can be misleading because it is not a true spectrum (function of frequency).

$$P(\lambda^2) = \int_{-\infty}^{+\infty} F(\phi) e^{2i\phi\lambda^2} d\phi, \quad (2)$$

so that  $F(\phi)$  can be expressed in a similar way:

$$F(\phi) = \frac{1}{\pi} \int_{-\infty}^{+\infty} P(\lambda^2) e^{-2i\phi\lambda^2} d\lambda^2. \quad (3)$$

$F(\phi)$  is a complex-valued function:

$$F(\phi) = |F(\phi)| e^{2i\psi_0(\phi)}, \quad (4)$$

where  $|F(\phi)|d\phi$  is the fraction of polarized flux that comes from regions of Faraday depth between  $\phi$  and  $\phi + d\phi$ ,  $\psi_0$  is the intrinsic polarization angle (perpendicular to the transverse component of the magnetic field,  $B_\perp$ ) and may itself depend on  $\phi$ .

Equation (3) lies at the heart of methods to recover  $F(\phi)$  from multi-frequency observations of the complex polarized intensity (called Rotation Measure, RM, synthesis; Brentjens & de Bruyn 2005). The RM synthesis has been used to recover Faraday components of compact sources (e.g. Mao et al. 2010) and diffuse structures in the Milky Way (e.g. Schnitzeler, Katgert, & de Bruyn 2009), in nearby galaxies (e.g. Heald, Braun, & Edmonds 2009) and in galaxy clusters (e.g. Pizzo et al. 2011). Several techniques have been proposed to deal with the limited  $\lambda^2$  coverage provided by real telescopes (RM-CLEAN; Heald 2009; sparse analysis and compressive sensing; Li et al. 2011, Andreut, Stil, & Taylor 2012; multiple signal classification; Andreut 2013) and with the missing negative  $\lambda^2$  (e.g. using wavelet transforms; Frick et al. 2010, 2011). Beck et al. (2012) also used wavelets to analyze the scales of structures in Faraday space and emphasized the need to combine data at high and low frequencies. Because of the difficulty of the RM synthesis technique to recover multiple Faraday components, it has been suggested to use direct  $q(\lambda^2)$  and  $u(\lambda^2)$  fitting, where  $q$  and  $u$  are the  $Q$  and  $U$  Stokes parameters normalised to the total intensity  $I$  (Farnsworth, Rudnick, & Brown 2011; O’Sullivan et al. 2012).

In this paper we show how observations, performed in the various wavelength ranges available at existing and planned radio telescopes, can be used to constrain the variation of  $\psi_0$  (and therefore the orientation of the magnetic field component perpendicular to the line of sight) with  $\phi$ . We use a Fisher matrix analysis to quantify the precision that can be achieved for fitted parameters and investigate the degeneracies that exist between the different constituents of our model. Recently, Ideguchi et al. (2014) performed a similar analysis to evaluate the capability of new radio telescopes to constrain the properties of intergalactic magnetic fields through observations of background polarized sources. Their work assumed two Faraday components, each with a constant  $\psi_0$ , a narrow one (the compact radio source) and a broad one (possibly associated with the Milky Way). Here we consider a linear variation of  $\psi_0$  with  $\phi$  and show how the degeneracies between pairs of model parameters can be broken using complementary datasets from different instruments in order to recover  $\psi_0(\phi)$ , using two simple models of  $F(\phi)$ , a constant and a Gaussian.

In the simple cases we consider, the variation of  $\psi_0(\phi)$  can be produced by a helical magnetic field. Magnetic helicity is a natural consequence of dynamo action and so-

phisticated statistical methods have been devised to try to infer its presence, although without inclusion of Faraday effects (Oppermann et al. 2011, Junklewitz & Enßlin 2011). Anomalous depolarization (an increase rather than the usual decrease of the degree of polarization with wavelength) produced by an helical field was discussed by Sokoloff et al. (1998). Helical fields have been invoked to explain the anomalous depolarization properties of the nearby galaxy NGC 6946 (Urbanik, Elstner, & Beck 1997) and polarization characteristics of the central part of the starburst galaxy NGC 253 (Heesen et al. 2011). Helical magnetic fields are also important in galactic and protostellar jets (e.g. Keppens & Meliani 2009, Fendt 2011). Bi-helical fields (with opposite signs of helicity on small and large scales) are produced in simulations of galactic dynamos and the signatures of such fields are discussed in a recent paper by Brandenburg & Stepanov (2014). In this paper, we focus on the detectability of single-helical magnetic fields.

## 2 ANALYSIS

### 2.1 Observables

We consider observations of the Stokes parameters  $Q$  and  $U$  with the instruments listed in Table 1. We used a nominal integration time of 1 h for the low-frequency observations (Giant Meterwave Radio Telescope, GMRT, Westerbork Synthesis Radio Telescope, WSRT, Low Frequency Array, LOFAR) and 10 min for observations with the more sensitive instruments (Jansky Very Large Array, JVLA, Australian Square Kilometre Array Pathfinder, ASKAP and Square Kilometre Array 1, SKA1). This allows an easy comparison of the sensitivities and makes it possible to display the confidence intervals of the parameters of interest on a common graph (Figs 2 and 3). We used a channel width of 1 MHz for all instruments except the JVLA for which a channel width of 2 MHz is more than sufficient in the wide S-band (2000–4000 MHz) to resolve the main features of the spectral energy distribution of the polarization. Note that all instruments allow the use of narrower channels; however, there is an obvious trade-off between sensitivity per channel and total integration time. We have varied the channel width over two orders of magnitude between 0.1 and 10 MHz and observed that the resulting precision on the main parameter of interest,  $\beta$  (equation (16)), changes by less than  $10^{-2}$  for a same total integration time of the SKA1-Survey. The quoted sensitivities are indicative since several instruments listed in Table 1 are still in their design phase. Also, some bands, especially the low-frequency ones, will be affected by radio frequency interferences and a fraction of the channels will be missing. With real data at hand it will be straightforward to include the actual frequency coverage and sensitivities in the modeling of a particular data set.

We scaled the sensitivities  $\sigma_{lit}$  quoted in the literature for a given effective bandwidth  $BW_{lit}$  and integration time  $t_{lit}$  to new values of the channel width  $\Delta\nu$  and integration time  $t_{int}$ , as given in the table, for a given number of tunings  $N_{tunings}$  to cover the whole bandwidth:

$$\sigma = \sigma_{lit} \sqrt{\frac{BW_{lit} t_{lit}}{\Delta\nu t_{int}} N_{tunings}}. \quad (5)$$

**Table 1.** Frequency range and sensitivity of the listed instruments. More details are given in Sect. 2.1.

Instrument	Note	Frequency band [MHz]	Sensitivity [mJy]	Channel width [MHz]	Integration time	Reference
JVLA	S-band	2000-4000	0.3	2	10 min	(1)
JVLA	L-band	1000-2000	0.6	1	10 min	(1)
ASKAP		700–1800	2.5	1	10 min	(2)
SKA1	Survey	650–1670	0.3	1	10 min	(3)
SKA1	Mid	350–3050	0.1	1	10 min	(3)
SKA1	Low	50–350	0.08	1	10 min	(3)
GMRT		580–640	0.5	1	1 hr	(4)
GMRT		305–345	3.8	1	1 hr	(5)
WSRT	92 cm	310–390	3.9	1	1 hr	(6)
LOFAR	HBA2	210–250	2.6–6.0	1	1 hr	(7)
LOFAR	HBA1	110–190	1.6	1	1 hr	(7)

(1) [science.nrao.edu/science/surveys/vlass/VLASkySurveyProspectus\\_WP.pdf](http://science.nrao.edu/science/surveys/vlass/VLASkySurveyProspectus_WP.pdf)(2) [www.atnf.csiro.au/projects/askap/spec.html](http://www.atnf.csiro.au/projects/askap/spec.html)(3) [www.skatelescope.org/wp-content/uploads/2013/03/SKA-TEL-SK0-DD-001-1\\_BaselineDesign1.pdf](http://www.skatelescope.org/wp-content/uploads/2013/03/SKA-TEL-SK0-DD-001-1_BaselineDesign1.pdf), page 18.(4) [www.ncra.tifr.res.in/ncra/gmrt/gmrt-users](http://www.ncra.tifr.res.in/ncra/gmrt/gmrt-users)

(5) Farnes (private communication).

(6) [www.astron.nl/smits/exposure/expCalc.html](http://www.astron.nl/smits/exposure/expCalc.html)(7) [www.astron.nl/radio-observatory/astronomers/lofar-imaging-capabilities-sensitivity-lofar-array/sensitivity-lofar-array](http://www.astron.nl/radio-observatory/astronomers/lofar-imaging-capabilities-sensitivity-sensitivity-lofar-array/sensitivity-lofar-array), table 4, for a 40-station Dutch array. Those numbers are preliminary, especially in the highest band.

The JVLA will be used to carry out sensitive surveys of large parts of the sky. We use figures provided by Steven T. Myers [National Radio Astronomy Observatory (NRAO)] in the Karl Jansky VLA Sky Survey Prospectus (see Table 1) for the JVLA in its B-configuration. In the S-band (2–4 GHz), the effective bandwidth (free from radio frequency interferences) is 1500 MHz, and a noise level of 0.1 mJy can be achieved in 7.7 seconds. The size of the synthesized beam is  $2.7''$  at the centre of the band. In the L-band (1–2 GHz), the effective bandwidth is 600 MHz and a noise level of 0.1 mJy can be achieved in 37 seconds of integration. The size of the synthesized beam is  $5.6''$ . In both cases we assumed a single tuning. We note that Mao et al. (2014) recently submitted a science white paper for a JVLA sky survey in the S-band (in the C-configuration), in which they consider several alternatives ranging from a shallow all-sky survey to ultra-deep fields of a few tens of square degrees. They estimate that a shallow all-sky survey of a total of about 3000 hours would lead to the detection of over  $2 \times 10^5$  polarized sources.

According to the ASKAP website, a continuum sensitivity of 29 to 37  $\mu\text{Jy beam}^{-1}$  for beams between  $10''$  and  $30''$  can be reached in 1 hour for a bandwidth of 300 MHz. Four tunings would be required to cover the whole frequency band from 700 to 1800 MHz, so in a total of 1 h a noise level of 1–1.3 mJy per 1 MHz channel would be reached. A major polarization survey with ASKAP (POSSUM) is in the design study phase.

In its first phase, the SKA will observe at low frequencies (50 – 350 MHz, SKA1-Low), mid-frequencies (0.35 – 3.05 GHz, SKA1-Mid) and in a survey mode in the 0.65 – 1.67 GHz range (SKA1-Survey). In 1 hour of observation and per 0.1 MHz channel, the sensitivity is expected to be 63  $\mu\text{Jy}$  for SKA1-Mid, 103  $\mu\text{Jy}$  for SKA1-Low, and 263  $\mu\text{Jy}$  for SKA1-Survey. We have assumed a single tuning for SKA1-Low and that for SKA1-Mid four tunings (in a 770 MHz bandwidth each) will be needed to cover the whole band; for SKA1-Survey, the maximum bandwidth will be

500 MHz, so two tunings will be needed. The corresponding noise levels per 1 MHz bandwidth and after 10 minutes of observations are given in Table 1.

For the GMRT 610 MHz band, our sensitivity estimate is based on the figures quoted by Farnes, Green, & Kantharia (2013) who reached a noise level in  $Q$  and  $U$  of 36  $\mu\text{Jy}$  per beam of  $24''$  in 180 minutes in a 16 MHz band centered at 610 MHz. Four tunings would be required to cover the whole band.

Our estimate of the sensitivity of the GMRT in the 325 MHz band relies on a noise level of 2.7 mJy per beam per 1 MHz channel in 1 hour, based on polarization observations of a pulsar done in 2011 (Farnes, private communication) and assuming that all 30 antennas would be available. Assuming that 2 tunings would be necessary to cover the whole band, this gives a noise level of 3.8 mJy in a total of 1 h.

The WSRT also operates in the 320 MHz band (called the 92 cm band). After 1 hour of observation, the theoretical noise level in Stokes  $I$  is 1.2254 mJy  $\text{beam}^{-1}$  in a 10 MHz band. This corresponds to about 3.9 mJy  $\text{beam}^{-1}$  in a 1 MHz channel. Note that confusion noise is expected to be significant in observations of the Stokes parameter  $I$  but it can be neglected  $Q$  and  $U$ . Gießbübel et al. (2013) recently detected polarization with the WSRT towards the Andromeda galaxy at 350 MHz.

The high-band array (HBA) of the LOFAR operates at frequencies between 110 MHz and 250 MHz with a filter between 190 and 210 MHz. LOFAR has detected polarization in the HBA and rotation measures could be inferred (e.g. in pulsars, Sotomayor-Beltran et al. 2013, and in polarized sources in the field of M 51, Mulcahy et al., in prep.). However, at the LOFAR frequencies depolarization is extremely strong and for the fiducial models presented in this paper the measurements at the quoted sensitivities do not provide improved constraints on the parameters related to the magnetic field. The LOFAR frequency coverage is displayed in

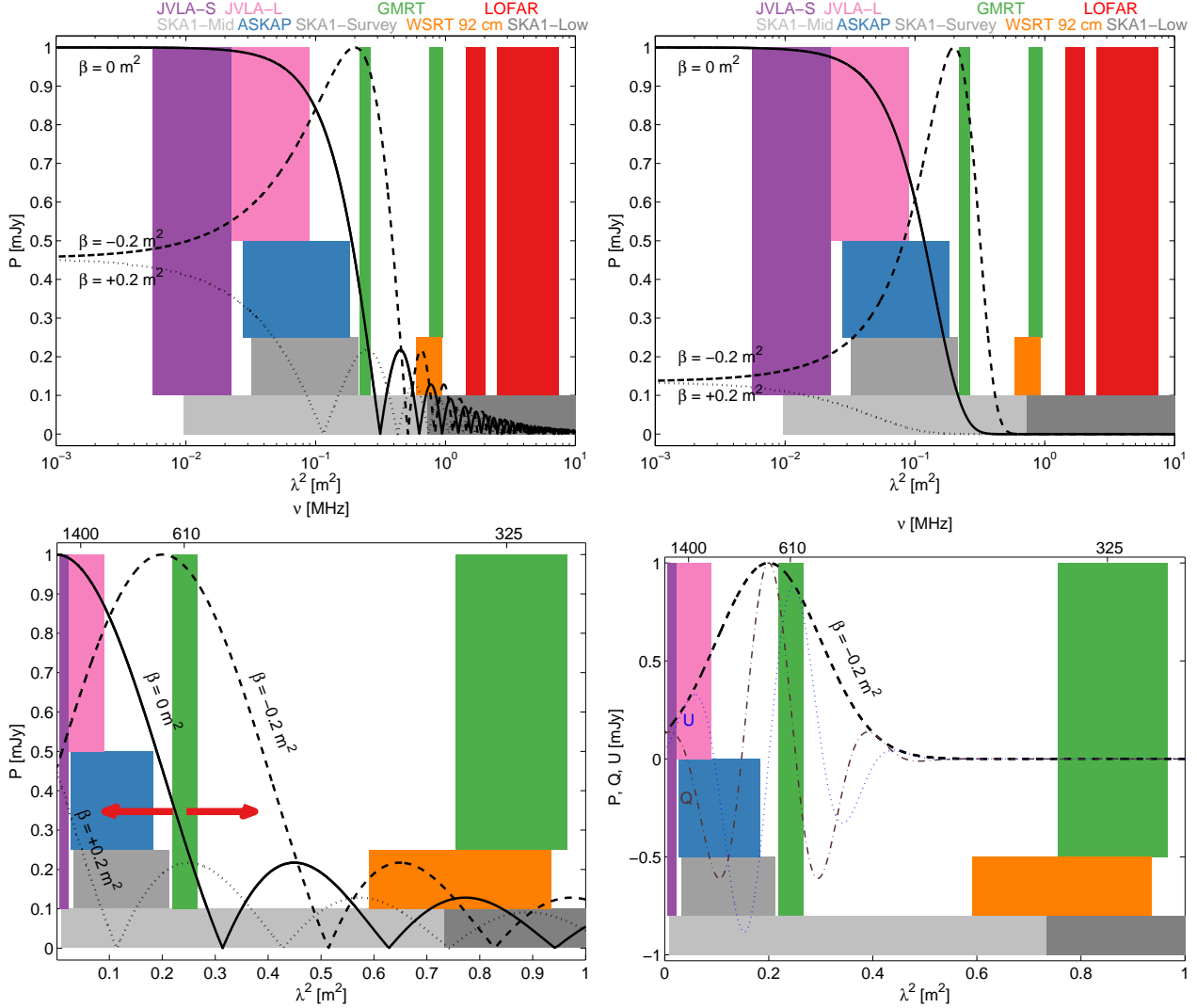


**Figure 1.** Polarized intensity versus  $\lambda^2$  for the top-hat model of the Faraday dispersion function (left) and the Gaussian model (right) for different values of the  $\beta$  parameter:  $\beta = 0$  (solid line),  $\beta = -0.2 \text{ m}^2$  (dashed line), and  $\beta = +0.2 \text{ m}^2$  (dotted line). The graphs on the top row are in semilogarithmic scale and extend out to the frequency bands of LOFAR, while the graphs on the bottom row are in linear scale and extend to a wavelength of about 1 metre, a band covered now by the GMRT and the WSRT and to be covered by the SKA. The wavebands of several instruments are shown in colour. For the Gaussian model, the variations of the Stokes parameters  $Q$  and  $U$  are also shown (bottom right panel, brown dotted-dashed and blue dotted lines) for the case with  $\beta = -0.2 \text{ m}^2$ . The pattern of polarized intensity is shifted horizontally as  $\beta$  varies, peaking at  $\lambda^2 = -\beta$ , as illustrated by the red arrows in the bottom left panel. A negative  $\beta$  ( $B_{\parallel}$  and handedness of  $B_{\perp}$  of opposite signs) results in a peak at  $\lambda^2 > 0$ , whereas a positive  $\beta$  results in increased depolarisation due to the combined depolarization effects of intrinsic helicity and Faraday rotation.

Fig. 1 but the LOFAR confidence intervals are therefore not shown in the other figures.

## 2.2 The Fisher matrix

The Fisher analysis is often used in cosmology (e.g. Albrecht et al. 2006, page 94). Consider a set of  $N$  data points and a model with  $P$  parameters,  $p_1, \dots, p_P$ . The Fisher matrix elements  $\mathcal{F}_{jk}$  are proportional to the second partial derivatives with respect to two given parameters of the likelihood function  $\mathcal{L}$  that the data set derives from the given model. If the measurement errors follow a Gaussian probability distribution, then

$$\mathcal{F}_{jk} = -\frac{\partial^2 \ln \mathcal{L}}{\partial p_j \partial p_k} = \frac{1}{2} \frac{\partial^2 \chi^2}{\partial p_j \partial p_k}, \quad (6)$$

where  $\chi^2$  is defined in Eq. (7). Denoting  $Q_{\text{mod}}$  and  $U_{\text{mod}}$  the values of the Stokes parameters  $Q$  and  $U$  for the assumed model, estimated at wavelengths  $\lambda_i$  and with noise levels  $\sigma_i$ , we have

$$\chi^2 = \sum_{i=1}^N \left( \frac{Q_i - Q_{\text{mod}}(\lambda_i; p_1, \dots, p_P)}{\sigma_i} \right)^2 + \left( \frac{U_i - U_{\text{mod}}(\lambda_i; p_1, \dots, p_P)}{\sigma_i} \right)^2. \quad (7)$$

The Fisher matrix elements can be written as

$$\mathcal{F}_{jk} = \sum_{i=1}^N \frac{1}{\sigma_i^2} \left( \frac{\partial Q_{\text{mod}}(\lambda_i^2; p_1, \dots, p_P)}{\partial p_j} \frac{\partial Q_{\text{mod}}(\lambda_i^2; p_1, \dots, p_P)}{\partial p_k} + \frac{\partial U_{\text{mod}}(\lambda_i^2; p_1, \dots, p_P)}{\partial p_j} \frac{\partial U_{\text{mod}}(\lambda_i^2; p_1, \dots, p_P)}{\partial p_k} \right). \quad (8)$$

The covariance matrix is the inverse of the Fisher matrix:

$$\sigma_{jk}^2 = (\mathcal{F}^{-1})_{jk}. \quad (9)$$

### 2.3 Models of $F(\phi)$ with linearly varying intrinsic polarization angle

We consider two simple models for  $F(\phi)$ , each with a linearly varying  $\psi_0$  as a function of Faraday depth:

$$\psi_0(\phi) = \alpha + \beta\phi, \quad (10)$$

with some constants  $\alpha$  and  $\beta$ . This is a parametrisation of  $\psi_0$  as a first-order polynomial and, as discussed below, it can also be interpreted as a helical magnetic field.

#### 2.3.1 Constant Faraday dispersion in the source

One of the simplest possible models for  $F(\phi)$  is the top-hat,

$$F(\phi; \mathbf{p}) = F_0 T(\phi; \mathbf{p}) e^{2i\psi_0(\phi; \mathbf{p})}, \quad (11)$$

where the set of parameters is  $\mathbf{p} = (F_0, \phi_0, \phi_m, \alpha, \beta)$ ,  $\psi_0(\phi; \mathbf{p})$  is given by Eq. (10) and  $T(\phi; \mathbf{p})$  is the top-hat function, with  $T = 1$  in the range  $\phi_0 - \phi_m < \phi < \phi_0 + \phi_m$  and  $T = 0$  elsewhere. The complex polarization is

$$P(\lambda^2; \mathbf{p}) = 2\phi_m F_0 \text{sinc}[2\phi_m(\lambda^2 + \beta)] e^{2i\psi(\lambda^2; \mathbf{p})}, \quad (12)$$

where

$$\psi(\lambda^2; \mathbf{p}) = \alpha + (\lambda^2 + \beta)\phi_0 \quad (13)$$

and  $\text{sinc}(x) = \sin(x)/x$ .

In a uniform slab, the Faraday depth varies linearly with the  $z$ -coordinate for  $\phi$  between  $\phi_0 \pm \phi_m$ :

$$\phi = 0.81 n_e B_{\parallel} z, \quad (14)$$

where  $n_e$  is in  $\text{cm}^{-3}$ ,  $B_{\parallel}$  in  $\mu\text{G}$ ,  $z$  in pc and  $\phi$  in  $\text{rad m}^{-2}$ .

Consider a magnetic field with a constant line-of-sight component, but with a rotating component in the plane of the sky:

$$B = \begin{pmatrix} B_{\perp} \cos(\alpha + k_H z) \\ B_{\perp} \sin(\alpha + k_H z) \\ B_{\parallel} \end{pmatrix}. \quad (15)$$

The intrinsic polarization angle clearly varies with the Faraday depth:

$$\psi_0 = \alpha + k_H z = \alpha + \beta\phi, \quad (16)$$

where

$$\begin{aligned} \beta &= \frac{k_H}{0.81 n_e B_{\parallel}} \\ &= 0.086 \text{ m}^2 \left( \frac{k_H}{2\pi \text{ rad kpc}^{-1}} \right) \left( \frac{0.03 \text{ cm}^{-3}}{n_e} \right) \left( \frac{3 \mu\text{G}}{B_{\parallel}} \right). \end{aligned} \quad (17)$$

For an helical field with  $k_H \simeq 2\pi \text{ rad kpc}^{-1}$ , we have  $\beta \simeq 0.1 \text{ m}^2$ .

Note that the sign of  $\beta$  depends on the relative orientation of the magnetic field component along the line of sight and the handedness of the helix. A positive  $\beta$  means that  $B_{\parallel}$ , which produces the Faraday rotation, and the intrinsic

rotation of  $B_{\perp}$  have the same direction. A negative  $\beta$  means that the Faraday rotation effectively counteracts the intrinsic rotation of the plane-of-sky magnetic field. This effect will be discussed further in Sect. 3.

#### 2.3.2 Gaussian Faraday dispersion function

As a simple alternative to the top-hat parametrisation of  $F(\phi)$  we also consider a Gaussian form,

$$F(\phi; \mathbf{p}) = F_0 \exp \left[ -0.5 \left( \frac{\phi - \phi_0}{\sigma_{\phi}} \right)^2 \right] e^{2i\psi_0(\phi; \mathbf{p})}, \quad (18)$$

where  $\mathbf{p}$  and  $\psi_0(\phi, \mathbf{p})$  are defined as before. This gives a complex polarization of

$$P(\lambda^2; \mathbf{p}) = \sqrt{2\pi} \sigma_{\phi} F_0 \exp \left[ -0.5 \left( \frac{\lambda^2 + \beta}{(2\sigma_{\phi})^{-1}} \right)^2 \right] e^{2i\psi(\lambda^2; \mathbf{p})}, \quad (19)$$

where  $\psi(\lambda^2; \mathbf{p})$  is given by Eq. (13). The modulus of  $P(\lambda^2)$  is a Gaussian centered at  $\lambda^2 = -\beta$  with variance  $\sigma^2 = (2\sigma_{\phi})^{-2}$ .

#### 2.3.3 General case

In the two previous sections we calculated  $P(\lambda^2)$  by integrating Eq. (2) analytically. Using the properties of the Fourier transforms, we now show why any linear variation of  $\psi_0$  with  $\phi$  produces a translation of the observed polarized intensity in the  $\lambda^2$  space.

Using the standard expression for Fourier transform (integral over  $t$  from  $-\infty$  to  $+\infty$  of a function  $f(t)$  times  $e^{-2\pi j \nu t}$  for the direct transform, and times  $e^{2\pi j \nu t}$  for its inverse), Eq. (2) can be written as

$$P(\pi \lambda^2) = \text{FT}^{-1} \{ F(\phi) \}, \quad (20)$$

where  $\text{FT}^{-1}$  is the inverse Fourier transform.

Using  $|F(\phi)| = F_c(\phi) * \delta(\phi - \phi_0)$  where  $F_c(\phi)$  is a real-valued function centered at  $\phi = 0$ ,

$$P(\pi \lambda^2) = \text{FT}^{-1} \{ F_c(\phi) * \delta(\phi - \phi_0) \cdot e^{2i(\alpha + \beta\phi)} \}. \quad (21)$$

The factor  $e^{2i\alpha}$  is independent of  $\phi$  and can be taken out of the integral. Multiplication becomes a convolution in the Fourier ( $\lambda^2$ ) space and convolution becomes a multiplication, so

$$P(\pi \lambda^2) = e^{2i\alpha} \text{FT}^{-1} \{ F_c(\phi) \} \cdot \text{FT}^{-1} \{ \delta(\phi - \phi_0) \} * \text{FT}^{-1} \{ e^{2i\beta\phi} \}. \quad (22)$$

Translation in the  $\phi$ -space gives a rotation in  $\lambda^2$ -space, and the inverse transform of the term involving  $\beta\phi$  becomes a delta-function, giving

$$P(\pi \lambda^2) = e^{2i\alpha} \left( \text{FT}^{-1} \{ F_c(\phi) \} \cdot e^{2i\pi\phi_0\lambda^2} \right) * \delta(\lambda^2 + \frac{\beta}{\pi}). \quad (23)$$

We then obtain

$$\begin{aligned} P(\pi \lambda^2) &= \left( \text{FT}^{-1} \{ F_c(\phi) \} e^{2i\alpha} \right) * \delta(\lambda^2 + \frac{\beta}{\pi}) e^{2i\pi\phi_0(\lambda^2 + \frac{\beta}{\pi})} \\ &= P_{\beta=0}(\pi(\lambda^2 + \frac{\beta}{\pi})) e^{2i\phi_0(\pi\lambda^2 + \beta)}, \end{aligned} \quad (24)$$

where  $P_{\beta=0}$  is the complex polarization corresponding to  $F_c(\phi)$  when  $\beta = 0$ . Changing the variable from  $\pi\lambda^2$  to  $\lambda^2$ , we obtain

$$P(\lambda^2) = P_{\beta=0}(\lambda^2 + \beta) e^{2i\phi_0(\lambda^2 + \beta)}, \quad (25)$$

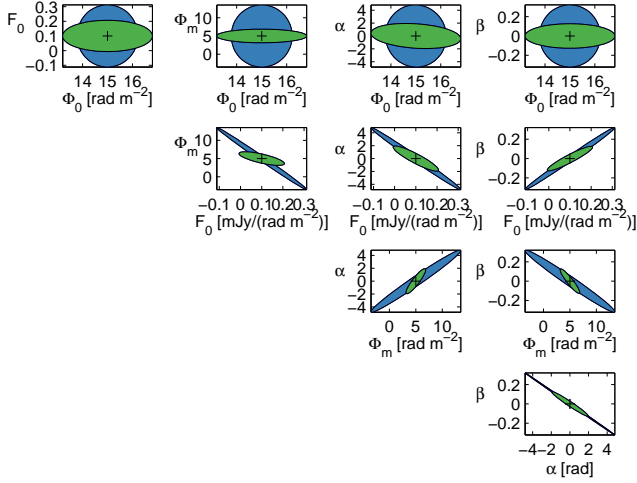


**Figure 2.** 68.3 per cent confidence regions for a top-hat model of the Faraday dispersion function when  $\beta = 0$ . The ASKAP regions are in blue and the GMRT ones in green.

so that

$$|P(\lambda^2)| = |P_{\beta=0}(\lambda^2 + \beta)|. \quad (26)$$

This shows that the observed modulus of the polarized intensity of a medium with a given  $\beta$  is simply a translation by  $\beta$  in  $\lambda^2$ -space of what would be observed if  $\beta$  were equal to zero.

$|F_c(\phi)|$  is real-valued, by definition; if it is even in  $\phi$ , its inverse Fourier transform is also real-valued, and the observed polarization angle will be

$$\psi(\lambda^2) = \alpha + \phi_0(\lambda^2 + \beta) \quad (27)$$

as found in Sect. 2.3.1 and 2.3.2 for the top-hat and the Gaussian cases.

## 2.4 Spectral dependence

The expressions of  $P(\lambda^2)$  used in the previous sections do not include any spectral dependence of the synchrotron emission. In general, the observed polarization can be written as the integral along the line of sight (los) and on a certain solid angle  $\Omega_b$  on the sky of the intrinsic polarization modulated by the Faraday rotation, where the intrinsic polarization is a fraction of the total emissivity of the source:

$$P(\lambda^2) = \int_{\text{los}} \int_{\Omega_b} d\lambda d\Omega \epsilon(\mathbf{r}, \lambda) \mathbf{p}_0(\mathbf{r}) e^{2i(\psi_0(\mathbf{r}) + \phi(\mathbf{r})\lambda^2)} \quad (28)$$

where the emissivity in the direction  $\mathbf{r}$ ,  $\epsilon(\mathbf{r}, \lambda)$ , may depend on  $\lambda$ , and  $p_0(\mathbf{r})$  is the intrinsic degree of polarization.

If the emissivity can be expressed as the product of two functions where one of them contains the spectral dependence (e.g.,  $\epsilon(\mathbf{r}, \lambda) = \hat{\epsilon}(\mathbf{r}) s(\lambda)$ ), then  $s(\lambda)$  can be taken out of the integral and Eq. (28) is invertible, following the same formalism as in Eqs (2) and (3) (for a discussion, see Sect. 3 of Brentjens & de Bruyn 2005).

In the calculation of the confidence intervals that can be obtained from observations in various wavebands, we modelled the spectral dependence as a power law,

$$s(\lambda) = \left(\frac{\lambda}{\lambda_0}\right)^{-\alpha_{\text{nth}}}, \quad (29)$$

with the normalisation wavelength  $\lambda_0 = 0.2$  m and a fixed non-thermal spectral index,  $\alpha_{\text{nth}} = -1$ . The values of the polarized intensity calculated using Eq. (2) were multiplied by  $s(\lambda)$ . This effectively increases the flux densities measured at  $\lambda > \lambda_0$  compared to the variations shown in Fig. 1, where no spectral dependence was included.

## 3 RESULTS

We use a fiducial top-hat model of the Faraday dispersion function with the following parameters:  $\phi_0 = 15$  rad m $^{-2}$ ,  $\phi_m = 5$  rad m $^{-2}$ ,  $F_0 = 0.1$  mJy/(rad m $^{-2}$ ),  $\alpha = 0$  rad, and three values of  $\beta$ , 0 and  $\pm 0.2$  m $^2$ . The total intrinsic polarized flux density (integrated over all Faraday depths) is thus  $2\phi_m F_0 = 1$  mJy. Because of depolarization, the signal expected at a given frequency will be weaker (see Figure 1) but should be detectable within a reasonable amount of observing time by current and future instruments (see Table 1). For comparison, we also use a Gaussian model of  $|F(\phi)|$  with the same total flux. The dispersion of the Gaussian is  $\sigma_\phi = \phi_m = 5$  rad m $^{-2}$  and the peak flux density per unit of Faraday depth  $2/\sqrt{2\pi} F_0 \simeq 0.08$  mJy/(rad m $^{-2}$ ). Note that  $\sigma_\phi$  characterises the Gaussian profile of the Faraday dispersion function for a model with a regular field, not to be confused with the dispersion in rotation measure (RM) caused by possible RM fluctuations across an observing beam (usually denoted  $\sigma_{\text{RM}}$ ). In Sect. 3.2 we discuss the additional depolarization effect by Faraday dispersion produced by a random field. The width of the Faraday structure (that is, the total Faraday depth, sometimes denoted  $\mathcal{R}$ , see Sect 3.2) in our fiducial top-hat model is  $2\phi_m = 10$  rad m $^{-2}$ . In many astrophysical cases this quantity can be larger (up to  $\sim 80$  rad m $^{-2}$  in spiral arms, e.g. Arshakian & Beck 2011). A larger total Faraday depth translates into a narrower “main peak” of the  $P(\lambda^2)$  distribution and weaker emission at long wavelengths.

### 3.1 Differential Faraday rotation versus magnetic field helicity

Fig. 1 shows the variation of the polarized intensity with  $\lambda^2$  for a top-hat (left column) and a Gaussian (right column) Faraday dispersion function. In the former case, the solid line ( $\beta = 0$ ) is the well-known sinc function produced by a uniform slab, which is more usually shown using the linear horizontal axis used in the bottom left panel. Note that, for clarity, the graphs in Fig. 1 do not include any spectral dependence of the intrinsic polarization. Figures 2 and 3 (the confidence regions of the parameters) do, on the other hand, include a spectral dependence of the form given by Eq. (29).

In the Gaussian case, the polarized intensity decreases monotonically and no emission is produced in the longer wavebands at which the GMRT and LOFAR operate (Fig. 1). In the bottom right panel we show the variation of the  $Q$  and  $U$  Stokes parameters (in brown and blue) for the Gaussian  $F(\phi)$ , which are the direct observables. They oscillate with a  $90^\circ$  phase shift with respect to each other.

In the rest of the paper we focus on the top-hat model because it gives stronger emission in longer wavebands for

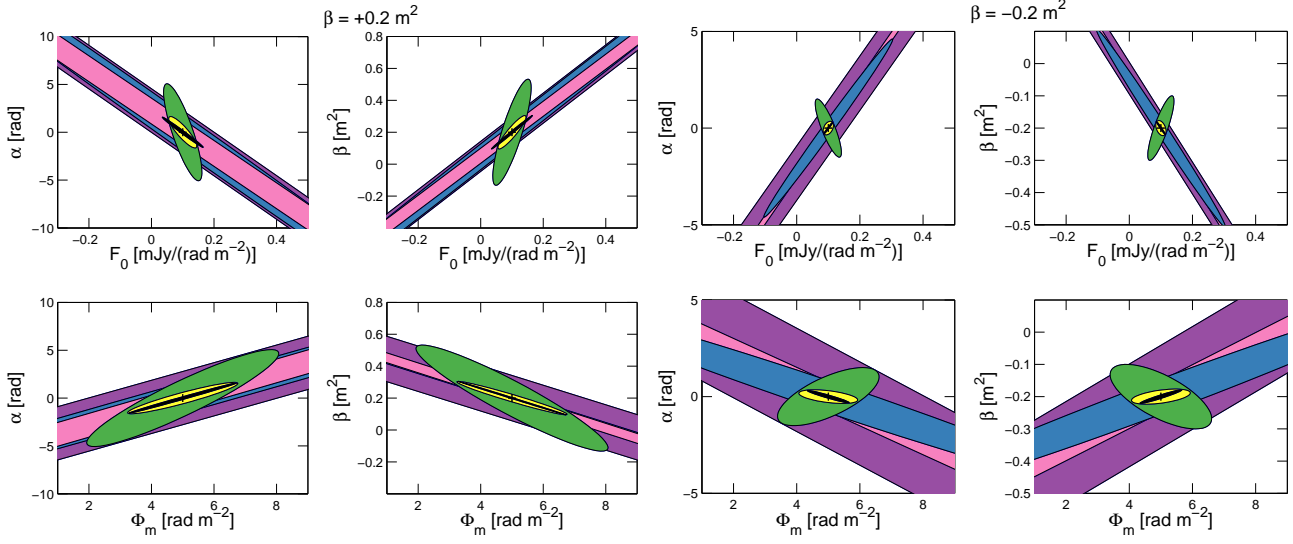


**Figure 3.** 68.3 per cent confidence regions for a top-hat model of the Faraday dispersion function for some of the instruments listed in Table 1. Left panel (four figures):  $\beta = +0.2 \text{ m}^2$ ; right panel (four figures):  $\beta = -0.2 \text{ m}^2$ . The yellow ellipses show the confidence regions obtained by combining an ASKAP (blue ellipses) and a GMRT (green ellipses) data set. The SKA1-Survey confidence ellipses are shown in black, and the JVLA ones in purple (S-band) and pink (L-band).

the parameters selected here and it includes the standard case for Faraday depolarization calculations of a uniform slab as a special case. It is most interesting to compare the variations of the polarized intensity for a positive and a negative  $\beta$ . When  $\beta > 0$ , the intrinsic helicity of the magnetic field and the Faraday rotation act in the same direction. This results in an increased depolarization at short wavelengths. Even for  $\lambda = 0$ , where Faraday depolarization is absent, the emission is significantly depolarized compared to the case of a constant magnetic field orientation ( $\beta = 0$ ). When  $\beta < 0$ , Faraday rotation counteracts the intrinsic rotation of the field, which means that the polarized emission peaks at a wavelength different from zero (dashed lines), where  $\lambda^2 = -\beta$  (eqs. (12) and (19)). This effect is similar to the “anomalous depolarization” discussed by Sokoloff et al. (1998, Section 9).

Fig. 2 shows the 68.3% confidence regions of the five different parameters obtained from the Fisher analysis for  $\beta = 0$ . The colour code is the same as in Fig. 1, with the ASKAP confidence regions in blue and the GMRT ones in green. The plots in the first row show that the central Faraday depth  $\phi_0$  is mostly uncorrelated with the other parameters. On the other hand,  $\phi_m$ , which describes the extent of the Faraday component in  $\phi$ -space, is strongly correlated with the parameters related to the intrinsic polarization angle ( $\alpha$  and  $\beta$ ) and at short wavelengths (in the ASKAP band) with the normalization of  $F(\phi)$  ( $F_0$ ). This is because the crucial effect is Faraday *differential* rotation across the Faraday component and not the magnitude of the central Faraday depth. An increase in  $\phi_m$  means stronger depolarization due to differential rotation which must be counteracted by a more negative  $\beta$  in order to produce a similar fit to the data. Vice versa, a lower  $\phi_m$  means weaker depolarization and  $\beta$  needs to become positive to increase the depolarization. In other words,  $\phi_m$  and  $\beta$  are anti-correlated around  $\beta = 0$ . Most importantly, the strength of the correlation between pairs of parameters including  $\alpha$  or  $\beta$  varies with the

selected waveband. This is what makes it possible to break parameter degeneracies by combining short-wavelength (like ASKAP) and long wavelength (like GMRT) data sets in order to better constrain the derived parameter values, as we discuss next.

Fig. 3 shows the one-sigma confidence ellipses for  $\alpha$ ,  $\beta$ ,  $F_0$  and  $\phi_m$  for  $\beta = +0.2 \text{ m}^2$  (four left panels) and  $\beta = -0.2 \text{ m}^2$  (four right panels). As expected, the orientation of the ellipses is similar for the short-wavelength instruments JVLA (S-band in purple and L-band in pink), ASKAP (blue) and SKA1-Survey (black). On the other hand, the long-wavelength GMRT data set (green) produces a different correlation between parameters; in some cases the confidence ellipses at short and long wavelengths are almost orthogonal, making it possible to reduce the confidence intervals on the derived parameter values considerably by using both wavelength ranges together (such as ASKAP and GMRT, shown in yellow). This is further illustrated in Fig. 4 where the precision that can be achieved in  $\beta$  for different instruments is shown. A combination of ASKAP and GMRT observations makes it possible to reach an uncertainty  $\Delta\beta < 0.25 \text{ m}^2$  if  $\beta < 0$ , for the integration times shown in Table 1 and the set of model parameters used. If  $\beta > 0$ , all signals are weaker because of increased depolarization and the precision on  $\beta$  (and all other model parameters) is lower.

### 3.2 Faraday dispersion

In this section we discuss the effect of depolarization by Faraday dispersion, due to possible random fluctuations of the magnetic field inside the synchrotron-emitting source. This effect was first discussed by Sokoloff et al. (1998) (Sect. 9) but they considered only the case of twisted fields where the rotation due to the helicity is counteracted by the

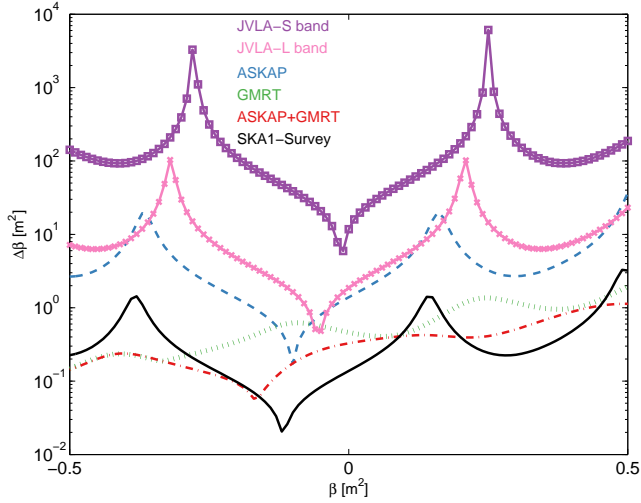


**Figure 4.** Precision that can be achieved on the  $\beta$  parameter as a function of  $\beta$  for observations with some of the instruments listed in Table 1. The combination of ASKAP and GMRT (shown here in dotted-dashed red) provides the smallest dependence of the uncertainty on  $\beta$ , comparable to what can be achieved with SKA1-Survey. Note, however, the difference in integration time (a total of 3 h for the joint ASKAP/GMRT observations versus 10 min for SKA1-Survey).

Faraday rotation ( $\beta < 0$  in our notation). As detailed in Appendix A, the observed complex polarized emission is

$$\langle P(\lambda^2) \rangle = e^{2i\Delta\psi_0} \frac{1 - e^{-S_H}}{S_H} \quad (30)$$

where

$$S_H = -2i(\mathcal{R}\lambda^2 - \Delta\psi_0) + 2\sigma_{\text{RM}}^2\lambda^4. \quad (31)$$

$\Delta\psi_0 = k_H L$  is the total rotation due to the helicity of the intrinsic polarization angle  $\psi_0$  across the thickness  $L$  of the slab,  $\mathcal{R}$  is the total Faraday depth of the source and  $\sigma_{\text{RM}}$  is the dispersion of the total Faraday depth. In the previous sections we had  $\mathcal{R} = 2\phi_m = 10 \text{ rad m}^{-2}$  and  $\Delta\psi_0 = 2\phi_m\beta = 0$  and  $\pm 2 \text{ rad} \simeq \pm 115^\circ$ . Figure 5 shows the variation of the polarized intensity with wavelength for the three cases considered before (a non-helical magnetic field ( $\beta = 0$ ) and helical magnetic fields with  $\beta = \pm 0.2 \text{ m}^2$ ) to which the effect of a random magnetic field component was added. The random fluctuations are described by values of  $\sigma_{\text{RM}}$  increasing from 0 (top, thicker curves) to  $10 \text{ rad m}^{-2}$  by step of  $2.5 \text{ rad m}^{-2}$ . The Faraday dispersion caused by the random fluctuations attenuates the variations and, for negative values of  $\beta$  where the intrinsic helicity acts in the opposite direction of the Faraday rotation, shifts the peak of the polarized intensity towards shorter wavelengths.

#### 4 SUMMARY

We examined how variations of the intrinsic polarization angle  $\psi_0$  with the Faraday depth  $\phi$  within a source affect the observable quantities. Using simple models for the Faraday dispersion  $F(\phi)$  and  $\psi_0(\phi)$ , along with the current and planned properties of the main radio interferometers, we show how degeneracies among the parameters describing

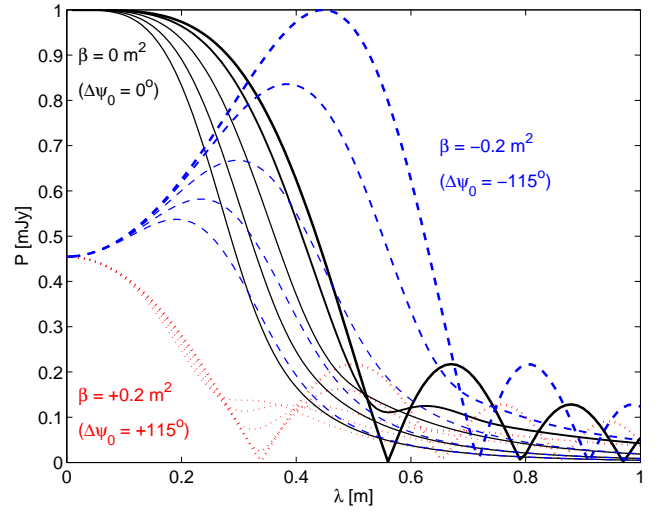


**Figure 5.** Variation of the polarized intensity with wavelength in the case of a uniform slab of Faraday depth  $\mathcal{R} = 10 \text{ rad m}^{-2}$  and Faraday dispersion characterised by  $\sigma_{\text{RM}} = 0, 2.5, 5, 7.5$  and  $10 \text{ rad m}^{-2}$  (curves from top to bottom) for  $\beta = 0$  (no helicity; black solid lines),  $\beta = +0.2 \text{ m}^2$  (red dotted lines) and  $\beta = -0.2 \text{ m}^2$  (blue dashed lines). The two latter cases correspond to a gradual change of the perpendicular component of the magnetic field by about  $115^\circ$  along the line of sight across the slab. The presence of a random field attenuates the variations and shifts the peak of the polarized emission towards shorter wavelengths.

the magneto-ionic medium can be minimised by combining observations in different wavebands. In particular we have shown that it may be possible to recover the sign and the magnitude of  $\beta$ , a parameter that we have defined and that is related to the relative effect of the helicity of the transverse magnetic field and the Faraday rotation due to the parallel component of the magnetic field. Since the direction of  $B_{\parallel}$  can be easily inferred from RM measurements, it should be possible to recover the sign (and, under some assumptions the magnitude) of the helicity of the magnetic field. However, the additional effect of Faraday dispersion by a random component of the magnetic field attenuates the variations of the polarized emission as a function of wavelength and may shift the peak of polarized emission towards shorter wavelengths if  $\beta$  is negative. Faraday depolarization effects (both by differential rotation and by dispersion) will have to be included in the modelling of real data in order to recover information on the helicity of the magnetic field. This approach is complementary to statistical studies of the correlation between the degree of polarization and the rotation measures of cosmic sources which may also provide information on magnetic helicity (Volegova & Stepanov 2010, Brandenburg & Stepanov 2014).

Planned surveys of fixed sensitivity will be biased towards radio sources with negative  $\beta$ , because of the depolarization produced when  $\beta > 0$ . Detection of  $\beta > 0$  will be more difficult both through  $Q(\lambda^2)$  and  $U(\lambda^2)$  model-fitting and RM synthesis because most of the signal is shifted toward negative  $\lambda^2$ . Brandenburg & Stepanov (2014) show that restricting the integral in Eq. (3) to the positive  $\lambda^2$  yields an erroneous reconstruction of  $F(\phi)$  when  $\beta > 0$ .

In this work we used a first-order parametrisation of the variation of intrinsic polarization angle with Faraday

depth. Higher-order representations could be used (or e.g. Chebyshev polynomials) if the data are of sufficient quality. Including a second-order term implies a convolution with an imaginary Gaussian and a significantly more complicated expression for  $P(\lambda^2)$ .

## ACKNOWLEDGMENTS

We thank Oliver Gressel for organizing the stimulating Nordita workshop ‘Galactic Magnetism in the Era of LO-FAR and SKA’ held in Stockholm in 2013 September. We also thank Axel Brandenburg and Rodion Stepanov for interesting discussions on the topics discussed in this paper and for sharing their related results with us. We are grateful to Rainer Beck, John H. Black, Jamie Farnes, George Heald, Anvar Shukurov and to the referee for constructive comments. AF is grateful to the Leverhulme Trust for financial support under grant RPG-097.

## REFERENCES

- Albrecht A., et al., 2006, *astro*, arXiv:astro-ph/0609591  
 Andrecut M., 2013, *MNRAS*, 430, L15  
 Andrecut M., Stil J. M., Taylor A. R., 2012, *AJ*, 143, 33  
 Arshakian, T. G., & Beck, R. 2011, *MNRAS*, 418, 2336  
 Beck R., Frick P., Stepanov R., Sokoloff D., 2012, *A&A*, 543, A113  
 Brandenburg, A., & Stepanov, R. 2014, arXiv:1401.4102  
 Brentjens M. A., de Bruyn A. G., 2005, *A&A*, 441, 1217  
 Burn B. J., 1966, *MNRAS*, 133, 67  
 Farnes J. S., Green D. A., Kantharia N. G., 2013, arXiv, arXiv:1309.4646  
 Farnsworth D., Rudnick L., Brown S., 2011, *AJ*, 141, 191  
 Fendt, C. 2011, *ApJ*, 737, 43  
 Frick P., Sokoloff D., Stepanov R., Beck R., 2011, *MNRAS*, 414, 2540  
 Frick P., Sokoloff D., Stepanov R., Beck R., 2010, *MNRAS*, 401, L24  
 Gießbübel, R., Heald, G., Beck, R., & Arshakian, T. G. 2013, *A&A*, 559, A27  
 Heald G., Braun R., Edmonds R., 2009, *A&A*, 503, 409  
 Heald G., 2009, *IAUS*, 259, 591  
 Heesen V., Beck R., Krause M., Dettmar R.-J., 2011, *A&A*, 535, A79  
 Ideguchi, S., Takahashi, K., Akahori, T., Kumazaki, K., & Ryu, D. 2014, *PASJ*, 66, 5  
 Junklewitz H., Enßlin T. A., 2011, *A&A*, 530, A88  
 Keppens, R., & Meliani, Z. 2009, *Protostellar Jets in Context*, 555  
 Li F., Brown S., Cornwell T. J., de Hoog F., 2011, *A&A*, 531, A126  
 Mao S. A., Gaensler B. M., Haverkorn M., Zweibel E. G., Madsen G. J., McClure-Griffiths N. M., Shukurov A., Kronberg P. P., 2010, *ApJ*, 714, 1170  
 Mao S. A., et al., 2014, arXiv, arXiv:1401.1875  
 O’Sullivan S. P., et al., 2012, *MNRAS*, 421, 3300  
 Oppermann N., Junklewitz H., Robbers G., Enßlin T. A., 2011, *A&A*, 530, A89  
 Pizzo, R. F., de Bruyn, A. G., Bernardi, G., Brentjens, M. A. 2011, *A&A*, 525, A104

- Schnitzeler D. H. F. M., Katgert P., de Bruyn A. G., 2009, *A&A*, 494, 611  
 Sokoloff D. D., Bykov A. A., Shukurov A., Berkhuijsen E. M., Beck R., Poezd A. D., 1998, *MNRAS*, 299, 189  
 Sotomayor-Beltran, C., Sobey, C., Hessels, J. W. T., et al. 2013, *A&A*, 552, A58  
 Urbanik M., Elstner D., Beck R., 1997, *A&A*, 326, 465  
 Volegova A. A., Stepanov R. A., 2010, *JETPL*, 90, 637

## APPENDIX A: FARADAY DISPERSION AROUND A MEAN HELICAL FIELD

In general, Eq. (2) can be rewritten as an integral along the line of sight of the intrinsic complex polarization modulated by the Faraday rotation:

$$P(\lambda^2) = \int_{\text{source}}^{\text{observer}} dz F(z) e^{2i\phi(z)\lambda^2}. \quad (\text{A1})$$

For a slab-like source of intrinsic polarized emission  $|F(z)| = 1/L$  between  $0 \leq z \leq L$  and intrinsic polarization angle  $\psi_0(z) = k_H z$ , it becomes

$$P(\lambda^2) = \frac{1}{L} \int_0^L dz e^{2i(k_H z + \phi(z)\lambda^2)}. \quad (\text{A2})$$

Our system of coordinates is chosen so that the origin is at the far end of the source and the observer is placed at  $+\infty$  (note that Burn 1966 placed the observer at the origin, where Sokoloff et al. 1998 used the symmetry plane of the slab as the origin of the reference frame, so that the source would extend from  $-L/2$  to  $+L/2$ . The choice of the origin of the reference system is of course arbitrary, but it introduces a phase in the final expression of the observed complex polarization).

We consider now the additional effect of Faraday dispersion produced by a random component of the magnetic field. The observed complex polarized intensity is

$$\langle P(\lambda^2) \rangle = \frac{1}{L} \int_0^L dz e^{2ik_H z} \langle e^{2i\phi(z)\lambda^2} \rangle, \quad (\text{A3})$$

where  $\langle \rangle$  denotes the ensemble average of the quantity between brackets:

$$\langle e^{2i\phi(z)\lambda^2} \rangle = \int_{-\infty}^{+\infty} d\phi p(\phi) e^{2i\phi(z)\lambda^2}, \quad (\text{A4})$$

where  $p(\phi)$  is the probability distribution function (PDF) of  $\phi$ .

The total magnetic field is the superposition of a regular component,  $\mathbf{B}$ , and a random one,  $\mathbf{b}$ . The scale on which the random field varies is denoted  $d$ . The components of the magnetic field along the line of sight are denoted

$$\mathbf{B}_{\text{tot}\parallel} = \mathbf{B}_{\parallel} + \mathbf{b}_{\parallel}. \quad (\text{A5})$$

Let us calculate  $p(\phi)$ . The Faraday depth at a given location  $z$  along the line of sight is

$$\begin{aligned} \phi(z) &= 0.81n_e \int_z^L dz (B_{\parallel} + b_{\parallel}) \\ &= \underbrace{m(L-z)}_{\text{regular}} + \underbrace{0.81n_e \int_z^L dz b_{\parallel}}_{\text{random}} \end{aligned} \quad (\text{A6})$$

where  $m = 0.81n_e B_{||} = \mathcal{R}/L$ , where  $\mathcal{R}$  is the total Faraday depth of the source. If  $b_{||}$  is a Gaussian variate, then  $\phi(z)$  is also a Gaussian variate<sup>2</sup>,  $p_G(\phi)$ , of mean  $m(L - z)$  and variance  $(0.81n_e b_{||} d)^2 \left(\frac{L-z}{d}\right) = v^2(L - z)$ , where  $v^2 = (0.81n_e b_{||})^2 d$ . Equation (A4) becomes

$$\langle e^{2i\phi(z)\lambda^2} \rangle = \int_{-\infty}^{+\infty} d\phi e^{2i\phi\lambda^2} p_G\left(\phi; \underbrace{\frac{\mathcal{R}}{L}(L-z)}_{\text{mean}}; \underbrace{v^2(L-z)}_{\text{variance}}\right). \quad (\text{A7})$$

This can be expressed as the inverse Fourier transform of the Gaussian PDF, which can be rewritten in a more convenient manner using the properties of the Fourier transform:

$$\begin{aligned} \langle e^{2\pi i \phi(z)\lambda^2} \rangle &= \text{FT}^{-1}\left\{p_G\left(\phi; 0; v^2(L-z)\right) * \delta\left(\phi - \frac{\mathcal{R}}{L}(L-z)\right)\right\} \\ &= \exp\left[-\frac{(2\pi\lambda^2)^2 v^2(L-z)}{2}\right] \cdot e^{2\pi i \frac{\mathcal{R}}{L}(L-z)\lambda^2} \end{aligned} \quad (\text{A8})$$

Replacing  $\pi\lambda^2$  by  $\lambda^2$ , and simplifying:

$$\langle e^{2i\phi(z)\lambda^2} \rangle = \exp\left[-\frac{S}{L}(L-z)\right], \quad (\text{A9})$$

where

$$S = \underbrace{-2i\mathcal{R}\lambda^2}_{\text{regular}} + \underbrace{2v^2 L\lambda^4}_{\text{random}}. \quad (\text{A10})$$

Finally Eq. (A3) becomes

$$\begin{aligned} \langle P(\lambda^2) \rangle &= \frac{1}{L} \int_0^L dz e^{2ik_H z} \exp\left[-\frac{S}{L}(L-z)\right] \\ &= e^{2i\Delta\psi_0} \left( \frac{1-e^{-S_H}}{S_H} \right), \end{aligned} \quad (\text{A11})$$

where  $\Delta\psi_0 = k_H L$  is the total rotation of the polarization angle across the slab and

$$S_H = -2i(\mathcal{R}\lambda^2 - \Delta\psi_0) + 2v^2 L\lambda^4. \quad (\text{A12})$$

Equation (A11) is a generalization of the expressions provided by Burn (1966) and Sokoloff et al. (1998) to the case of Faraday dispersion around an helical field.  $v^2 L$  is the variance of the total Faraday depth of the source and is usually denoted  $\sigma_{\text{RM}}^2$ .

<sup>2</sup> Note that Burn (1966) had a factor  $d/2$  instead of  $d$  in his expression of the variance, which resulted in a factor of 2 in the “random” term of  $S$  (see Eq. (A12)), as also noted by Sokoloff et al. (1998).